

Preliminary Results from Detector-Based Throughput Calibration of the CTIO Mosaic Imager and Blanco Telescope Using a Tunable Laser

Christopher W. Stubbs, Sara K. Slater, Yorke J. Brown, Daniel Sherman

*Department of Physics
Harvard-Smithsonian Center for Astrophysics
Harvard University
17 Oxford Street
Cambridge
MA 02138
USA*

R. Chris Smith, Nicholas Suntzeff, Abi Saha
*Cerro Tololo Interamerican Observatory
NOAO
Casilla 603
La Serena
Chile*

John L. Tonry, Joseph Masiero, Stephen Rodney
*Institute for Astronomy
University of Hawaii
2680 Woodlawn Drive
Honolulu
HI, 96822
USA*

Abstract. We describe the scientific motivation for achieving photometric precision and accuracy below the 1% level, and we present a calibration philosophy based on using calibrated *detectors* rather than celestial *sources* as the fundamental metrology reference. A description of the apparatus and methodology is presented, as well as preliminary measurements of relative system throughput vs. wavelength for the Mosaic imager at the CTIO Blanco 4m telescope. We measure the throughput of the optics, filter, and detector by comparing the flux seen by the instrument to that seen by a precisely calibrated monitor photodiode, using a tunable laser as the illumination source. This allows us to measure the transmission properties of the system, passband by passband, with full pupil illumination of the entire optical train. These preliminary results are sufficiently promising that we intend to further pursue this technique, particularly for next-generation survey projects such as PanSTARRS and LSST.

1. Introduction and Motivation

The challenge of photometry is to extract knowledge of the location and flux distribution of astronomical sources, based on measurements of the 2 dimensional distribution of detected photons in a focal plane. Each pixel i in the detector array sees a signal S_i given by

$$S_i = \sum_{\text{sources } j} \int \Phi_j(\lambda) R_i(\lambda) T(\lambda) A_i d\lambda, \quad (1)$$

where the sum is taken over all sources (including the sky) that contribute to the flux in the pixel, $\Phi_j(\lambda)$ is the photon spectrum for source j , $R_i(\lambda)$ is the throughput of the pixel, including the transmission of the optics and the pixel's quantum efficiency, $T(\lambda)$ is the optical transmission of the atmosphere, and A_i is the effective aperture of the system for pixel i , essentially the wavelength-independent part of the instrumental response.

Traditional flat-fielding techniques attempt to extract knowledge of $\Phi(\lambda)$ from this array of sums of integrals by first dividing the flux in each pixel by a scalar number, F_i^B , the “flat field” for that pixel in a passband B . It is however clear from the above equation that this is not arithmetically correct if multiple sources with different photon spectra are contributing to the flux in the pixel. Furthermore, airmass corrections typically assume that the atmospheric transmission for a given band B depends only on the secant of the zenith angle, ignoring any wavelength dependence across the passband. Astronomical instruments are currently calibrated, in practice, using celestial calibrators. At present the most popular photometric system is based on our knowledge (Hayes75) (Hayes75b) (Castelli et al. 1994) of Vega. Our observational information about the spectrum of Vega is of course fundamentally based upon the terrestrial blackbody sources against which Vega was itself calibrated, by ground-based measurements. Present work, described elsewhere in this volume, uses a combination of photospheric modeling and observation to construct a synthetic spectra of spectrophotometric calibration objects. Since we don't know the distances or radii of the sources well enough to determine what their apparent fluxes should be, there is an overall multiplicative ambiguity that is (for Vega-based magnitude systems) tied to a monochromatic flux of Vega. This in turn links all celestial calibrators to the terrestrial blackbody sources that were used in the calibration of Vega.

Considerable careful effort has been expended on building a network of spectrophotometric stars across the sky (Oke83) (Colina & Bohlin 1994) (Hamuy et al. 1992) (Hamuy et al. 1994) (Bohlin 1996) (Megessier 1995). These stars, in conjunction with the network of secondary photometric standards (Landolt 1992), form the basis for determining the instrumental throughput of different instruments, and for making the photometric transformations into a “standard” system (Fukugita et al. 1996).

The current state of the art with this approach produces flux measurements with fractional uncertainties at the few percent level (Abazajian et al. 2004) (Bessell 1999) (Bessell 2005). Considerable further progress along these lines is described in other contributions to this conference.

A variety of forefront scientific issues motivate breaking through the 1% barrier that has long been a limitation in the precision of ground-based photom-

etry. One example, which has in large part motivated the work described here, is the Dark Energy problem. Type Ia supernovae are a powerful probe of the history of cosmic expansion (Riess et al 1995) (Perlmutter et al 1996), and they provide strong evidence for the existence of the Dark Energy. As we move from the detection to the characterization of Dark Energy, the challenge is detecting subtle signals in the Hubble diagram. In particular, measuring the equation of state parameter $w = P/\rho$ of the Dark Energy requires confidence in photometry at or below the 1% level.

The fundamental measurement in supernova cosmology is a determination of apparent brightness vs. redshift. In order to measure brightness in the same spectral region for each supernova, we must shift to redder passbands for supernovae at increasing redshifts. Any systematic miscalibration of the photometric zeropoints in different passbands would produce a corresponding systematic distortion in the Hubble diagram. Furthermore, a detailed knowledge of the instrumental response function is required, in order to properly account for the effects of the redshifted SN spectrum as seen in the passbands used (i.e. to perform “K corrections” (Peacock98)).

An alternative approach, which we intend to pursue, is to *measure* the quantities $R_i(\lambda)$, each pixel’s response vs. wavelength, and $T(\lambda)$, the optical transmission of the atmosphere for each image. We have described the formalism of this approach elsewhere (Stubbs & Tonry 2006) and we encourage the reader to consult that paper in conjunction with this one, which describes a preliminary implementation of this technique. In Stubbs & Tonry (2006) we point out (for a major wide field survey which will measure many of current photometric standards as a matter of course) the merits of reporting all photometric survey results in the “natural” photometric system of the survey, rather than inflicting the systematic errors introduced by transferring measurements into a “standard” system.

In particular we intend to fully exploit the fact that we can obtain detectors whose response vs. wavelength can be far better characterized (Larason 1998) than the spectrum of a calibration source.

The measurement of atmospheric transmission is another essential ingredient in this approach, which is a topic of current research (Adelman et al. 1996) (Granett et al. 2005), but we will not address that issue here.

2. Throughput Measurements of the CTIO Mosaic Imager and the Blanco 4m Telescope

The preliminary results described here were obtained in Dec 2005, in a run that was undertaken to test the feasibility of the approach.

Our system uses the well-characterized detection efficiency of a NIST-calibrated photodiode as the “laboratory standard” against which we calibrate the apparatus. The quantum efficiency (QE) of the device as a function of wavelength is shown in Figure 1.

An overall conceptual diagram of the arrangement of the apparatus is shown in Figure 2. We project light from a tunable laser onto the flat-field screen in the dome. We measure the flux reflected from the screen, incident on the telescope pupil, with a calibrated photodiode. We then compare the flux detected by the

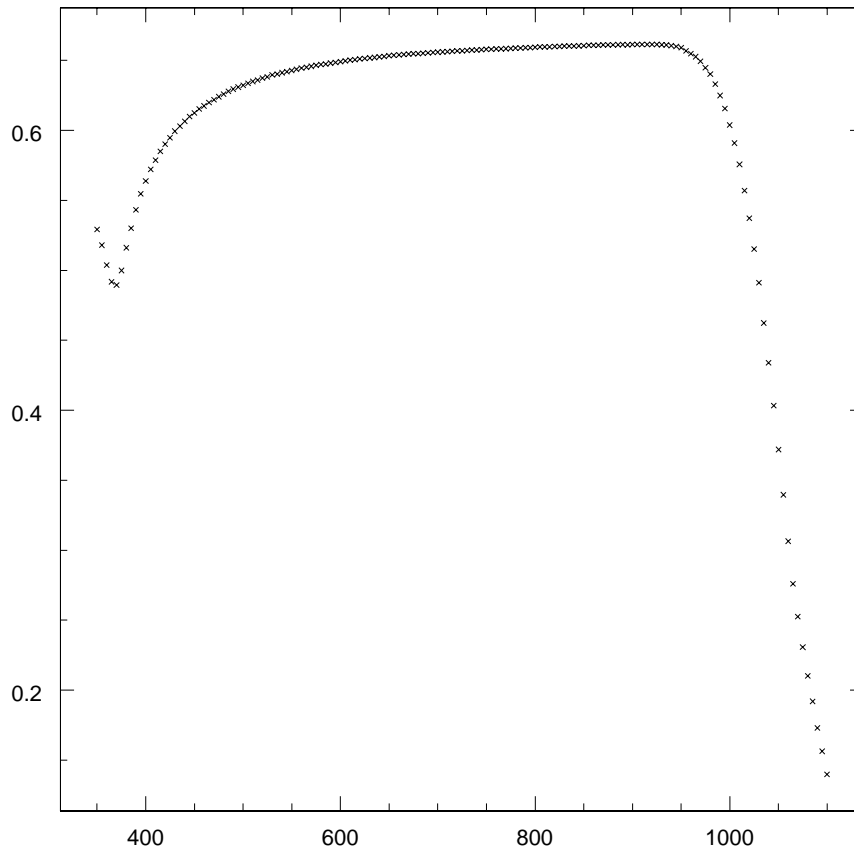


Figure 1. Quantum Efficiency Curve for NIST Photodiode. This plot shows the photon detection efficiency vs. wavelength for a Hamamatsu 2281 photodiode. The curve is dominated by the index of refraction mismatch between Silicon and air; the internal QE is essentially unity for most of the spectral regime of interest. The lack of structure and the fact that the detector response can be calibrated at the 10^{-4} level makes these devices attractive as fundamental metrology standards.

instrument to the incident flux, as measured by the photodiode. Performing this measurement at a succession of wavelengths allows us to determine system throughput as a function of wavelength, using the calibrated photodiode as the fundamental reference.

2.1. The Blanco Telescope and the Mosaic II Prime Focus Imager

We define the imager to include the detectors, dewar window and filters. The primary mirror and the prime focus corrector optics are considered as part of the telescope.

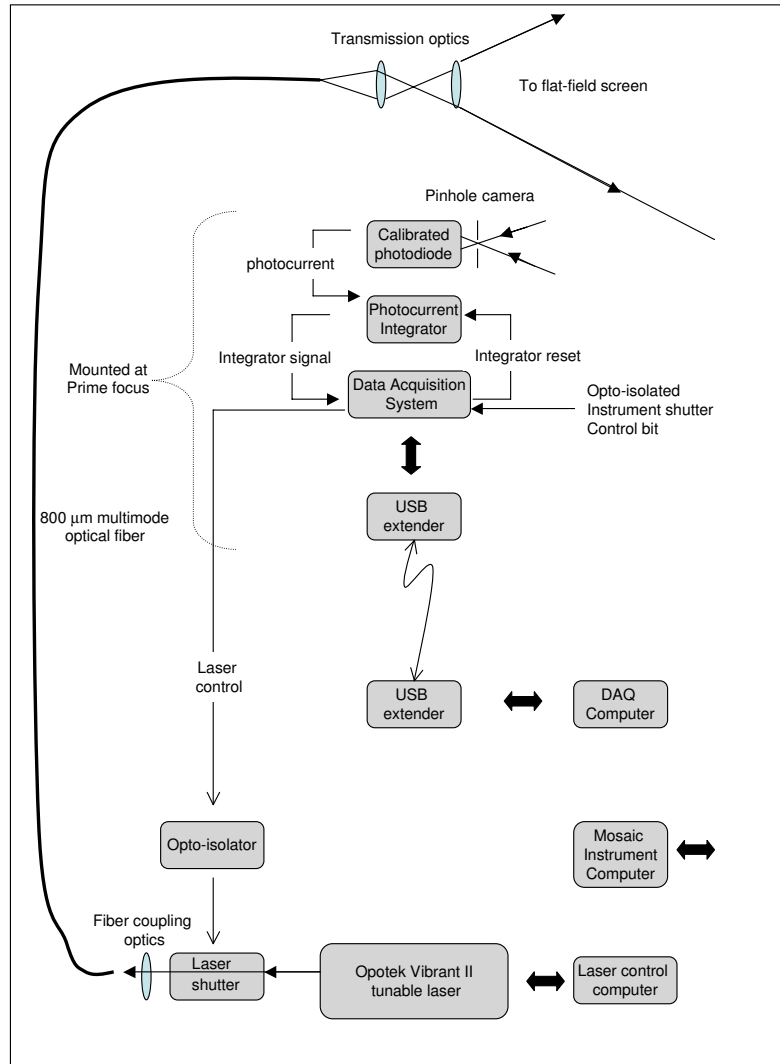


Figure 2. Schematic diagram of calibration system configuration. Monochromatic light from the tunable laser is projected onto the full-aperture flat-field screen. The calibrated photodiode is used to monitor the total laser light delivered to the input pupil of the 4m Blanco telescope, using timing information derived from the Mosaic camera’s shutter bit.

The Blanco Telescope Long a mainstay of Southern hemisphere astronomy, the Blanco telescope uses a 4m hyperbolic primary mirror to deliver light to (in our configuration) the prime focus. The $f/2.5$ beam is presented to a triplet correc-

tor that contains an atmospheric dispersion compensator (ADC). When feeding prime focus, the telescope optics comprise one reflection from the Aluminium-coated primary mirror, plus four compound optical elements (the 3 corrector lenses plus the ADC).

For the program described here we rotated the ADC to its “neutral” position, which corresponds to no correction for atmospheric dispersion.

The Mosaic II Imager The Mosaic II imager comprises a total of eight back-illuminated 2048 x 4096 pixel CCDs, with 15 μm pixels that subtend 0.26 arcsec on a side. The total field of view of the system is 0.6 x 0.6 degrees. Each detector is typically read out from two amplifiers, producing a multi-extension FITS file with 16 layers (two amplifiers for each of eight detectors). The CCD output stage and Arcon characteristics limit the pixel read rate to about 50 Kpix/sec, resulting in a readout time of 120 sec for an unbinned image. This readout time dominates our overall throughput in acquiring a stack of calibration images, since our typical flat-field exposure time is 10 sec.

The instrument has a filter changing mechanism that contains up to 14 large-format filters. Some of these are colored glass composites, and others are interference filters. We also have the ability to use a blank glass “dummy” filter that retains the optical prescription by inserting a piece of fused silica glass in place of a filter.

While there is some variation across the detectors in the Moasic array, typical characteristics are listed in Table 2.1.. Details are available from the online documentation that is maintained by CTIO. Dark current is negligible.

Table 1. Typical Mosaic Imager Characteristics

Parameter	Typical Value
Read Noise	6 electrons
Gain	2 electrons/ADU
Saturation (min)	60,000 electrons
Crosstalk between amplifiers	10^{-3}

For the calibration data described here, we were careful to keep the signal levels within the linear regime for the most restrictive of the detectors.

2.2. Calibration Apparatus

The tunable laser was located in a room within the 4m dome, to shield it from temperature changes and from dust. An 800 micron diameter multimode optical fiber with low OH content, clad in semirigid conduit, carried the laser light up through the telescope structure and onto an optical bench assembly that was mounted on the top of the prime focus cage. This optical bench held the optics for illuminating the flat-field screen, the calibration diode, the photocurrent integration electronics, and our A/D converter. A USB extender carried digital signals between this location and the data acquisition and control computer that was located near the laser. Computers for controlling the laser and the Mosaic instrument were also placed at this location.

We illuminated the full area of the flat-field screen by sending light that emerged from the fiber optic through a pair of lenses. Each unvignetted element of area dA on the flat-field screen illuminates every pixel of the imager, since the optical system maps angles at the pupil to position in the focal plane. The camera sees all rays that emerge within a cone of opening angle $\sqrt{2} \times 0.3^\circ = 0.42^\circ$. If the screen emission is approximated as a Lambertian, then the most extreme ray has an intensity relative to the central ray of $I(\text{edge})/I(\text{center}) = \cos(0.42^\circ) = 0.9999$. Although we would have ideally mapped out the Bi-Directional Reflectance Function (BDRF) of the flat-field screen as a function of wavelength, this was impractical as the flat-field screen surface was at an inaccessible height in the dome.

2.3. Flat-field Screen Illumination.

We used a Vibrant II tunable laser (manufactured by Opotek of Carlsbad CA) as a tunable source of monochromatic light. The laser uses a 20 Hz Nd:YAG laser at 1.064 microns as the source of photons. This light passes through a pair of non-linear optical crystals that upconvert the light into photons at $\lambda=355$ nm. These UV photons are then run through an optical parametric oscillator (OPO) that downconverts each UV photon into a pair of photons, conserving both energy and momentum. The orientation of the OPO crystal relative to the incident beam can be adjusted so as to select for a specific wavelength of interest. The wavelength of the output beam can thereby be tuned over a wavelength range of 400 nm to 2 μm .

From the photon pair produced, the upper or lower frequency beam is selected by exploiting the fact that these two beams have orthogonal linear polarizations. Our light source produces 5 nsec wide pulses at 20 Hz, with typical energies of 10-50 mJ per pulse. We measured a power of 10 mW going into the fiber at $\lambda=800$ nm when we adjusted the power to give 30,000 ADUs of typical signal in the Mosaic pixels. There is a “degeneracy point” in the OPO system at $\lambda=710$ nm where the OPO output is not well behaved, but this is a very narrow spectral avoidance region and did not pose a problem.

We also use optical filters to ensure that there is no contamination from the partner photon, or from the UV beam. We measured the spectral contamination from the partner photon to be less than one part in 10^3 .

The light intensity from the laser is adjustable in two ways. The Nd:YAG laser has a variable time delay between the flashlamp pulse and the Q-switch driven dump of the laser cavity. Changing this time delay varies the intensity of the light emitted by the Nd:YAG laser. In addition we installed an actuated polarizer on the output of the OPO stage, that can be used to modify the intensity of the monochromatic light downstream of the OPO. We used a combination of these to generate a desired intensity of light from the tunable laser. Since the conversion efficiency of the OPO system does depend on wavelength, we found the ability to adjust the output intensity to be an important feature of the illumination system.

The light from the tunable laser was focussed onto a multimode optical fiber which was run through the telescope structure and up to the prime focus cage. The output end of the fiber was attached to an optical bench that was mounted on the upper end of the prime focus cage. The 800 micron output tip

of the fiber was then imaged onto the flat-field screen, making a spot that filled roughly 75% of the screen area.

Although the light emitted from the laser is polarized, as the light is transmitted through the optical fiber its polarization becomes randomized. The coherence length of the pulsed laser light is sufficiently short that speckle effects were unobservable.

2.4. Monitoring light at the input pupil with Calibrated Photodiode

We configured a NIST-calibrated Silicon photodiode as a pinhole camera. By avoiding any imaging optics we avoid introducing any unwanted wavelength dependence in the calibration signal chain.

Ideally the calibration diode would monitor the entire emitting area of the flat-field screen over the angular range seen by the camera system, but this was not practical: we have a standoff distance of about 4 m between the flat-field screen and the calibration detector. We had the choice between configuring the diode to monitor the entire screen area over a wider angle, or narrowing the calibration diode's field of view and monitoring a portion of the screen area. We elected to configure the diode to monitor the full illuminated region of the screen, and adjusted the pinhole spacing to accomplish this.

2.5. Electronics and Instrument Interface

The system elements include a data acquisition module which was connected to a computer through a USB extension module. This allowed our main system components (except for the laser) to be mounted on the top end ring of the telescope.

Taking a dome flat image with the Mosaic camera, and more specifically the opening of the Mosaic shutter, initiated a data taking sequence. The shutter control bit was therefore passed through an opto-isolation stage and then monitored by our data acquisition module.

The photodiode output was sent into an integrator circuit that we used to monitor the integrated dose of light received by the screen. This integrative approach was important in minimizing any deleterious effects due to pulse-to-pulse intensity variations in the laser output. The integrator output was connected to one of the analog inputs on the data acquisition module. The integrator was reset on command using one of the digital outputs on the data acquisition module.

We used one laptop computer to control the tunable laser, a second to run the Mosaic camera, and a third one to communicate with the data acquisition system.

2.6. Data Acquisition Sequence

We rotated the Atmospheric Dispersion Corrector (ADC) to the neutral position, and pointed the telescope to the nominal location of the flat-field screen. We then acquired calibration images according to the following prescription, iterating through wavelength:

1. We selected the filter of interest.

2. We adjusted the laser wavelength to the desired value, changing the polarizer and wavelength “cleanup” filter as appropriate.
3. We adjusted the flashlamp to Q-switch delay and the attenuator setting on the Opotek laser while monitoring the light intensity with the monitor photodiode, to provide uniform intensity. This also ensured that we delivered the full light dose during the 10 sec interval while the Mosaic shutter was open.
4. We took a “laser on” dome flat exposure with the Mosaic imager, with a typical exposure time of 10 sec. As described above our electronics monitored the shutter status bit and once the Mosaic shutter is fully open first reset the photocurrent integrator and, after a half second delay, we open the laser shutter and allow the laser light to strike the flat-field screen. The integrated signal from the photodiode is monitored by our data acquisition system, and once a calibrated dose of photons is delivered to the input pupil of the telescope we close the laser shutter. We are careful to ensure that the laser shutter closes before the Mosaic shutter. This eliminates potential systematic effects from the Mosaic shutter. We stored both the FITS file from the Mosaic imager as well as the time history of the integral of the flux seen by the photodiode.
5. We then took a “laser off” exposure with the Mosaic imager, in order to measure the ambient light contamination in our flats. In our processing we subtract these adjacent “laser-off” images in order to use only the laser light contributions to the flats. We again store the associated time history of the photodiode flux.
6. We then changed to the next wavelength of interest, and iterated the procedure.

2.7. Representative Raw Data

Figure 3 shows a typical measurement of the integrated light intensity seen by the photodiode. The plot shows the ambient and laser light contributions. The laser intensity is at least ten times that of the ambient light in the dome.

An amusing example of a pair of images from the Mosaic instrument is shown in Figure 4, which clearly shows the spatial modulation of device QE that is responsible for “fringing” due to night sky emission lines. At longer wavelengths the fractional variation in a pixel’s QE over wavelength can be as large as 10%.

Figure 4 illustrates that spatial variation in QE not only produces additive problems arising from bright sky lines, which are traditionally removed through fringe corrections, but also introduce subtle variations in effect wavelength response across the array which are manifested as spatial variations in the effective passband. It is awkward that the spatial scale of the fringing variations is matched to the size of a typical PSF. For astronomical sources with spectra that are not flat, this spatial QE variation is not properly corrected for by using broadband flats. For example the photometry reported for an emission line object could vary by as much as 10%, depending on where on the array the object is located. Furthermore, this effect suggests that narrowband imaging is

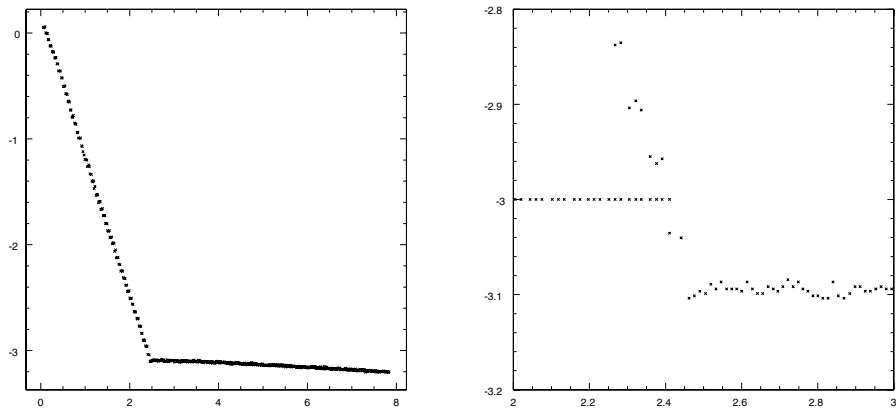


Figure 3. Integrated signal from photodiode. These plots show the integrated photodiode signal in arbitrary units vs. time (in sec). More light drives this signal more negative. The left hand panel shows the integrated light at the photodiode over an entire image, where the steep region is with the laser on and the flatter region is after laser shutoff. The laser light clearly dominates over the ambient light in the dome, even in the daytime. We did linear fits to distinguish between the contributions from ambient and laser light. The right hand panel is an expansion of the time around laser shutoff. The individual laser pulses are clearly visible. The horizontal line at the -3 level is the laser shutter command bit status.

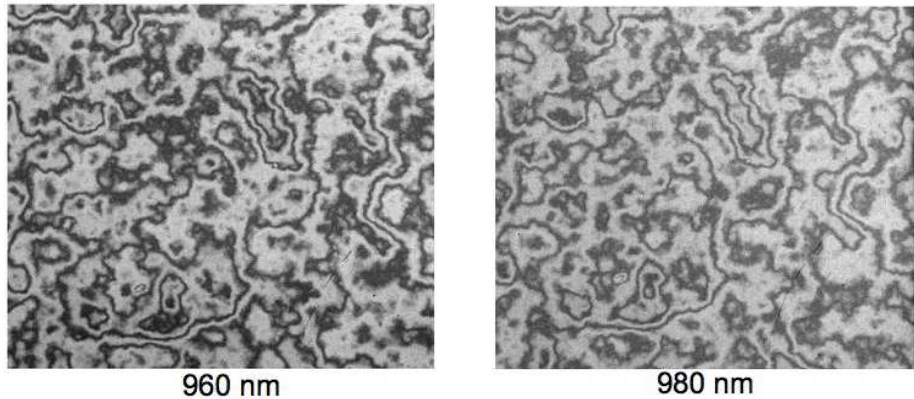


Figure 4. Fringing Measured by Monochromatic Laser Illumination. These two panels compare the fringing pattern at $\lambda=960$ nm and $\lambda=980$ nm. Note the variation in phase of the fringing pattern between these two wavelengths. Data such as these should allow us to construct high accuracy fringe frames for flatfielding, in conjunction with sky emission spectra.

more compromised than broadband imaging, where many cycles of fringing are averaged over, across the optical passband.

3. Data Processing

3.1. Calibration Signal Processing

We stored the calibration photocurrent signal before, during and after the laser shutter was opened. As shown in Figure 3 we did linear fits to determine the ambient light intensity, $\Phi_{ambient}^{diode}$, in ADUs per second. We subtracted this from each data point and used the linear fit to the integrated photocurrent to determine the total integrated laser light dose $I_{laser}^{diode}(\lambda)$ (in ADUs) for each measurement. Dividing this value by the diode QE provides us with a number that is proportional to the number of photons delivered to the input pupil; $N_{laser}(\lambda) = \frac{I_{laser}^{diode}(\lambda)}{QE(\lambda)}$.

3.2. Processing of the CCD Images

The images, both laser-on and laser-off, were corrected for bias levels using the pixel overscan regions. The laser-off images showed only a very slow variation over time, in agreement with the ambient light levels reported by the calibration diode. The difference between laser-on and laser-off images produced an image array $F(i, j, \lambda)$ that contains a measurement of throughput for each pixel (i, j) at the wavelength λ .

3.3. Determination of System Throughput

For each wavelength we took the ratio $T(i, j, \lambda) = \frac{F(i, j, \lambda)}{N_{laser}(\lambda)}$ to determine each pixel's sensitivity at the wavelength λ . We took a 100 x 100 pixel region in one of the amplifiers to generate the representative results shown here. Figure 5 shows throughput vs. wavelength when the filter is replaced by a fused silica blank. We also show the vendor's QE (at room temperature) for a device that is representative of those mounted in the Mosaic camera.

We took multiple data sets at $\lambda=800$ nm in order to (1) determine repeatability and (2) ascertain whether the results depended upon the total light dose. Changing the light dose by a factor of two had no measurable effect. The throughput measurements are reproducible to better than 1%.

4. Preliminary Conclusions, and Next Steps

We consider the preliminary results we obtained to be sufficiently promising to proceed with this calibration scheme. We note that the alternative approach we are pursuing does not in any way compromise or collide with reducing survey data with standard techniques. In fact comparing the results with the two methods will provide useful constraints on systematic effects.

Our near term goal is to obtain a full set of throughput calibration data for the various filters on the Mosaic instrument, by the end of 2006. We also will

- Develop and refine atmospheric transmission measurement techniques,
- Develop and refine self-luminous flat field screens, as described in the companion paper by Brown et al in these proceedings,
- Continue to work towards implementing these techniques for both PanSTARRS and LSST.

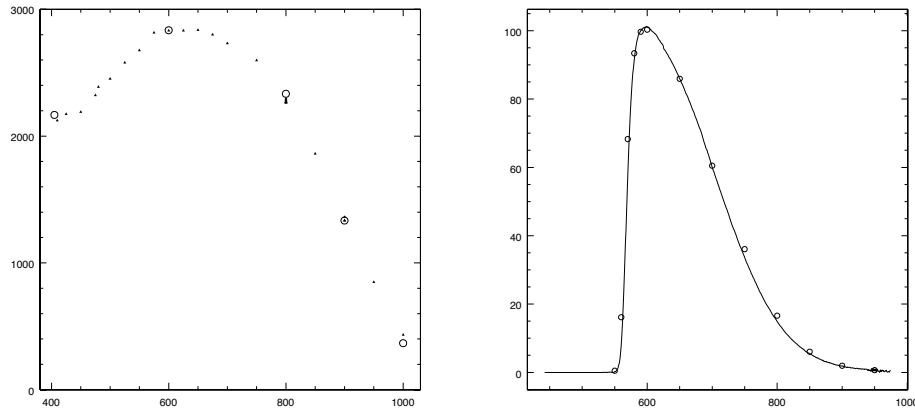


Figure 5. Throughput with Fused Silica Blank Filter and R band filter sanity check. The left panel shows relative system throughput (in arbitrary units) vs. wavelength in nm, obtained with a fused silica blank in place of a filter. The solid points are the data we obtained and the open circles are the vendor’s room temperature measurements of the detector QE. We multiplicatively scaled our data by single overall normalization in order to drive agreement at $\lambda=600$ nm. The right panel shows a consistency check of R band filter throughput. We took throughput data with the R band filter, made from a stack of Schott glasses, and divided it by the blank glass throughput curve shown in left panel. This ratio should reproduce the throughput of the R band filter alone. The right hand figure shows (as circles) our data while the solid line is the the transmission curve for this filter from the documentation maintained at CTIO. The good agreement shows that this approach of in-situ, full aperture throughput determination is promising.

Acknowledgments. We are grateful to the US National Science Foundation, under grants AST-0443378 and AST-0507475, for their support of this work in the context of the ESSENCE supernova survey. We are also grateful to the LSST Corporation, Harvard University, and the US Department of Energy Office of Science for their support of the continuing development of these techniques. The work described here would not have been possible without the skill and support of the technical staff at CTIO. We are also very grateful to Dr. Eli Margalith of Oportek for his support and assistance in this endeavor.

References

- Abazajian et al, 2004, AJ, 128, 502.
 Adelman, S. I. and Gulliver, A. F. and Holmgren, D. E., 1996 ASP Conf. Ser. 108: M.A.S.S., Model Atmospheres and Spectrum Synthesis, 293
 Bessell, M. S., 1999, PASP, 111, 1426
 Bessell, M. S. 2005 ARA&A, 43 293.
 Bohlin, R. C., 1996, AJ, 111, 1743
 Castelli, F. and Kurucz, R. L., 1994, A&A, 281, 817
 Colina, L. and Bohlin, R. C., 1994, AJ, 108, 1931
 Fabregat, J. and Reig, P., 1996, PASP, 108, 90

- Fukugita, M., Ichikawa, T., Gunn, J. E., Doi, M., Shimasaku, K. and Schneider, D. P., 1996, AJ, 111, 1748
- Granett, B.R., Chambers, K.C. and Magnier, E. BAAS 207 17318 2005.
- Hamuy, M., Walker, A. R., Suntzeff, N. B., Gigoux, P., Heathcote, S. R. and Phillips, M. M., 1992, PASP, 104, 533
- Hamuy, M., Suntzeff, N. B., Heathcote, S. R., Walker, A. R., Gigoux, P. and Phillips, M. M. 1994, PASP, 106, 566
- Hartman, J. D., Bakos, G., Stanek, K. Z. and Noyes, R. W. 2004, astro-ph/0405597
- Hayes, D. S. and Latham, D. W., 1975, ApJ, 197, 593
- Hayes, D. S. and Latham, D. W. and Hayes, S. H., 1975, ApJ, 197, 587
- Landolt, A., 1992, AJ, 104, 340
- Larason, T.C., Bruce, S. and Parr, A., 1998, Spectroradiometric Detector Measurements, US Dept of Commerce.
- Megessier, C., 1995, A&A, 296, 771
- Oke, J. B. and Gunn, J. E., 1983, ApJ, 266, 713
- Peacock, J., *Cosmological Physics*, 1998, Cambridge University Press
- Perlmutter, S. et al, 1996 ApJ 517, 565
- Riess, A. et al, 1995 AJ 116, 1009.
- Stubbs, C. W. and Tonry J. L. , 2006, ApJ, 646, 1436.